remote sensing

MDPI

Article

Recovering Bathymetry Using BP Neural Network Combined with Modified Gravity–Geologic Method: A Case Study in the South China Sea

Xiaodong Chen [1,2], Min Zhong [1,3,*], Mingzhi Sun [1,2], Dechao An [1], Wei Feng [1,3] and Meng Yang [1,2,3]

[1] School of Geospatial Engineering and Science, Sun Yat-sen University, Zhuhai 519082, China; chenxd97@mail2.sysu.edu.cn (X.C.); sunmzh5@mail2.sysu.edu.cn (M.S.); andch@mail2.sysu.edu.cn (D.A.); fengwei@sysu.edu.cn (W.F.); yangmeng5@mail.sysu.edu.cn (M.Y.)
[2] Key Laboratory of Marine Environmental Survey Technology and Application, Ministry of Natural Resources, Guangzhou 510300, China
[3] Key Laboratory of Comprehensive Observation of Polar Environment, Ministry of Education, Sun Yat-sen University, Zhuhai 519082, China
* Correspondence: zhongm63@mail.sysu.edu.cn

Abstract: The gravity–geologic method (GGM) is widely used for bathymetric predictions. However, the conventional GGM cannot be applied in regions without actual bathymetric data. The modified gravity–geologic method (MGGM) enhances the accuracy of bathymetric models by supplementing short-wavelength gravity anomalies with an a priori bathymetric model, but it overlooks the significance of actual bathymetric data in the prediction process. In this study, we used the BP neural network (BPNN), incorporating shipborne depth soundings and coastline data as zero-depth estimates combined with the MGGM to produce a bathymetric model (BPGGM_BAT) for the South China Sea (105°E–122°E, 0°N–26°N). The results indicate that the BPGGM_BAT model decreases the root-mean-square (RMS) of bathymetry differences from 154.33 m to approximately 140.43 m relative to multibeam depth data. Additionally, the RMS differences between the BPGGM_BAT model and multibeam depth data show further improvements of 19.63%, 20.10%, and 19.54% when compared with the recently released SRTM15_V2.6, GEBCO_2022, and topo_V27.1 models, respectively. The precision of the BPGGM_BAT model is comparable to that of the SDUST2023BCO model, as verified using multibeam depth data in open sea regions. The BPGGM_BAT model outperforms existing models with RMS differences of 8.54% to 32.66%, as verified using Electronic Navigational Chart (ENC) bathymetric data in the regions around the Zhongsha and Nansha Islands. A power density analysis suggests that the BPGGM_BAT model is superior to the MGGM_BAT model for predicting seafloor topography within wavelengths shorter than 15 km, and its performance is closely consistent with that of the topo_V27.1 and SDUST2023BCO models. Overall, this integrated method demonstrates significant potential for improving the accuracy of bathymetric predictions.

Keywords: seafloor topography; BPNN; GGM; satellite altimetry; gravity anomaly

check for updates

Citation: Chen, X.; Zhong, M.; Sun, M.; An, D.; Feng, W.; Yang, M. Recovering Bathymetry Using BP Neural Network Combined with Modified Gravity–Geologic Method: A Case Study in the South China Sea. *Remote Sens.* **2024**, *16*, 4023. https://doi.org/10.3390/rs16214023

Academic Editor: Sergei Badulin

Received: 16 October 2024
Revised: 27 October 2024
Accepted: 27 October 2024
Published: 29 October 2024

Copyright: © 2024 by the authors. Licensee MDPI, Basel, Switzerland. This article is an open access article distributed under the terms and conditions of the Creative Commons Attribution (CC BY) license (https://creativecommons.org/licenses/by/4.0/).

1. Introduction

High-precision bathymetry in the South China Sea (SCS) is fundamental for geophysical and plate tectonic research in the region [1], and it is crucial for maritime activities such as transportation, fishing, mineral resource exploitation, and military operations. Traditional bathymetric measurement uses sonar equipment to provide high-resolution depth data, but it remains inefficient [2]. According to the theory of isostasy, marine gravity anomalies primarily arise from variations in the morphology of seafloor topography and the density distribution of its compensatory materials, exhibiting a strong correlation with seafloor topography [3,4]. Currently, marine gravity anomaly data obtained through

altimetry technology are instrumental in facilitating broad-scale seafloor topography inversion, serving as a primary method for supplementing uncharted areas in global seafloor mapping [5–8].

With advancements in high-precision marine gravity field data and increased shipborne bathymetric data, seafloor topography inversion methods have been optimized and improved. The commonly used methods include the Inverse Nettleton method (also known as the Smith and Sandwell method, SAS) [9,10], GGM [8,11–15], the least squares collocation method [16], and deep learning methods [17–19]. The GGM predicts bathymetry with high accuracy, fast computation speed, and suitability for large areas. These attributes contribute to its widespread use in seafloor topography inversion. Kim et al. [11] applied the conventional GGM to invert the bathymetry of the Drake Passage in Antarctica. This highlighted that the accuracy of GGM in seafloor topography inversion is primarily influenced by the number of actual depth control points, the precision and resolution of gravity anomaly data, and the impact of density contrast differences between seawater and ocean bottom rock. Modeling long-wavelength and short-wavelength gravity anomalies is crucial for performing seafloor topography inversion with the GGM. Typically, the conventional GGM interpolates actual bathymetric data to derive long-wavelength gravity anomalies. However, in areas with sparse shipborne bathymetric data, this interpolation process may introduce errors.

Utilizing published seafloor topography models and actual depth measurements as prior information can effectively reduce errors in the conventional GGM. For example, based on the topo_V19.1 model from the Scripps Institution of Oceanography (SIO), Xing et al. [20] employed a three-dimensional rectangular prism model to more accurately simulate short-wavelength gravity anomalies, integrating a Tikhonov regularization method and multiple geophysical constraints. While this method significantly enhances the conventional GGM, it remains too inefficient. Using the Inverse Nettleton method to construct a linear seafloor topography model, Xu et al. [10] presented a novel adaptive nonlinear iterative (ANI) method designed to predict seafloor topography from altimetry-derived gravity data in the SCS. The results demonstrated significant improvements in model accuracy, particularly in regions with complex seafloor features. Hsiao et al. [12] proposed the MGGM, which constructs an altimeter-only bathymetric model over the SCS. The method estimates bathymetric results in the SCS by accounting for differences between the reference gravity field and high-precision gravity anomaly fields. To derive a reference long-wavelength gravity anomaly field, the MGGM applies low-pass filtering to data from the pre-existing topo_V17.1 model rather than using depth control points and interpolation to construct a reference long-wavelength gravity anomaly field, as is typical for the GGM. However, the MGGM does not consider the contribution of shipborne bathymetric depth data. Additionally, it mainly considers linear relationships divided by a Bouguer term to obtain an improved short-wavelength depth, which may result in a less accurate bathymetry model.

Classic bathymetric inversion methods, such as the GGM and the Inverse Nettleton method, rely on density contrast or regression coefficients, primarily restoring bathymetric information based on a linear relationship between gravity anomalies and seafloor topography [10]. However, this relationship is nonlinear owing to factors like seafloor geology. Beyond existing bathymetric inversion methods, deep learning offers a fast and highly accurate way of predicting bathymetry, particularly in capturing signals from nonlinear terms [21,22]. Meanwhile, by relying solely on unprocessed gravity data, deep learning may fail to accurately capture the relationships in sensitive coherent bands between gravity anomalies and seafloor topography, reducing accuracy in seafloor topography models. Sun et al. [23] detrended and filtered gravity anomalies and vertical gravity gradients, using an improved BPNN to construct seafloor topography in the Mariana Trench area. Compared with the conventional GGM, the BPNN-estimated model reduced the standard deviation (STD) and RMS of discrepancies with multibeam check data by 16.53 m and 20.79 m, respectively. Yang et al. [24] combined conventional GGM-derived short-

wavelength gravity anomalies with a retrained Fully Connected Deep Neural Network (FC-DNN) to reconstruct a seafloor topography model in the Gulf of Guinea. Their FC-DNN with short-wavelength gravity anomalies reduces the STD of bathymetry differences by up to 13.3% compared with the conventional GGM. Furthermore, they demonstrated that short-wavelength gravity anomalies play a significant role in enhancing accuracy.

In this study, we used the BPNN and the MGGM to predict seafloor topography models. The MGGM utilizes parameters such as long-wavelength topographic fields, long-wavelength gravity fields, and short-wavelength gravity fields, all of which are closely correlated with actual bathymetric data. Meanwhile, the BPNN integrates actual bathymetric data and certain nonlinear terms with gravity anomalies, addressing some of the limitations of the MGGM. Section 2 introduces the data utilized in this study, along with the principles and processes of the MGGM and BPNN methods. Section 3 presents the inversion results and accuracy assessment of the models, with the discussion focusing on their accuracy and the performance of the power spectral density (PSD). The final section presents the conclusions and recommendations for future research.

2. Data and Methods

The study area is the SCS (105°E–122°E, 0°N–26°N), located at the convergence of the Eurasian, Pacific, and Indo-Australian plates, one of the largest marginal seas along the East Asian margin. The data used in this study include gravity data and depth data.

2.1. Data Sources

2.1.1. Global Marine Gravity Anomaly Models

The quality of satellite altimetry-derived gravity anomalies determines the accuracy of seafloor topography obtained through the MGGM. The primary global marine gravity anomaly models include the Sandwell and Smith (S&S) series from the SIO [25] and the DTU series from the Technical University of Denmark [26]. The NSOAS series from Northeastern University [27] and the SDUSTGRA series from Shandong University of Science and Technology [28–30] also offer sufficient precision for high-accuracy seafloor topography inversion [31,32].

The precision and spatial resolution of SDUST2022GRA were evaluated against other published altimeter-derived global gravity anomaly models (DTU17, V32.1, and NSOAS22) and shipborne gravity measurements, achieving a global precision of 4.43 mGal and representing an improvement of approximately 0.22 mGal over existing models [33]. In an SCS region characterized by numerous islands and reefs with a complex coastline and near-shore structure, SDUST2022GRA showed an enhancement of 0.16–0.24 mGal compared with the other models. These assessments suggest that SDUST2022GRA is a reliable global marine gravity anomaly model. It is expected to enhance the inversion accuracy of seafloor topography models by utilizing the high-precision SDUST2022GRA model and leveraging its near-shore accuracy advantages. Thus, this study employs global marine gravity anomalies from the SDUST2022GRA model (Figure 1a) and the EGM2008 model expanded to spherical harmonic degree 2160 (Figure 1b) as a reference gravity anomaly model. The difference between the marine gravity anomalies and the reference gravity anomalies can be primarily observed along coastlines, around islands, and over deep-sea seamounts.

2.1.2. Shipborne Depth Data and Coastline Data

The seafloor topography models constructed by the BPNN and MGGM incorporate actual depth data, including shipborne single-beam data, multibeam sounding data, and coastline data used for zero-depth estimates (Figure 2a). We utilized single-beam bathymetry data and multibeam sounding grid data from the National Centers for Environmental Information (NCEI) for seafloor topography inversion. Within the study area, we downloaded 2,347,831 single-beam bathymetric points and 36,939,090 multibeam bathymetric sounding grid points. Owing to the varying measurement time and quality of the

shipborne data, we used the GEBCO2023 model as a reference seafloor topography model to filter outliers in the bathymetric measurements. The "grdtrack" module of the Generic Mapping Tools (GMT) version 6.2 software [34] was used for outlier removal to obtain depth differences from the GEBCO2023 model at each bathymetric point through spline interpolation. We then removed shipborne sounding points where differences exceeded triple the STD and relative errors were above 0.5. This process eliminated 10,437 outliers from the single-beam bathymetry points and 707,326 outliers from the multibeam sounding grid data points.

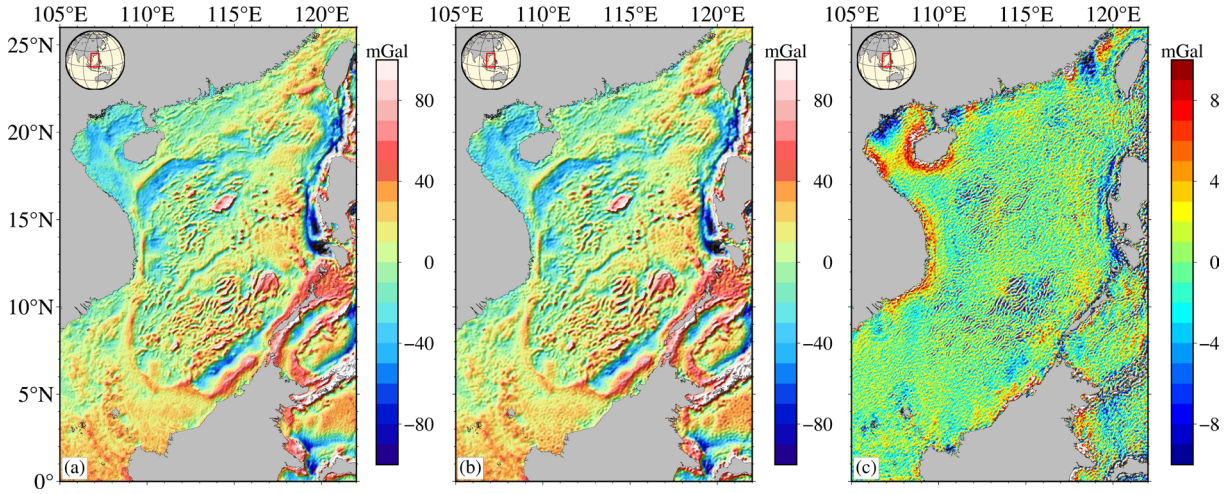


Figure 1. Gravity anomalies in the SCS: (**a**) the SDUST2022GRA model; (**b**) the EGM2008 model. (**c**) Differences between the SDUST2022GRA model and the EGM2008 model.

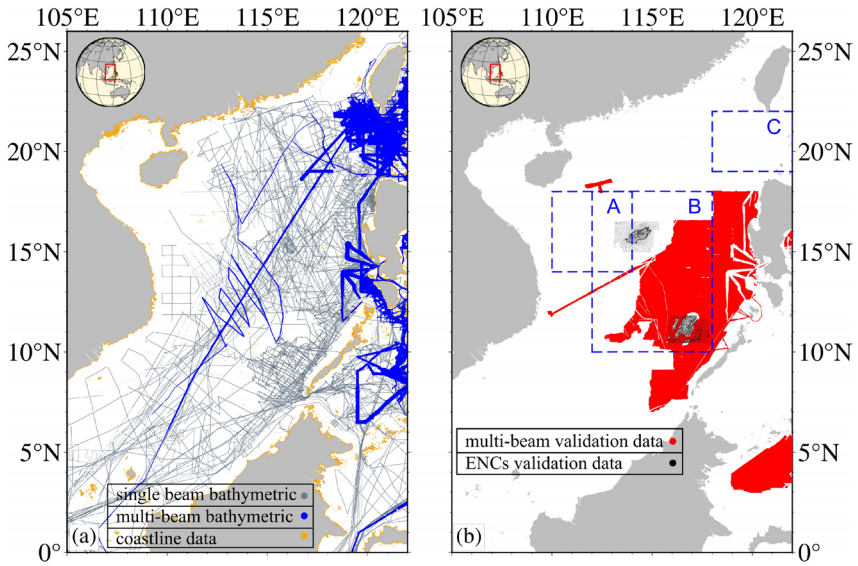


Figure 2. Depth data distribution map: (**a**) the slate-gray dots, blue dots, and orange dots denote control points; (**b**) the red dots and black dots denote check points, the three areas A, B, and C, marked by blue dashed boxes, are designated for analyzing the power spectrum of the models.

Commonly used coastline data are derived from the GSHHG model from GMT. OpenStreetMap (OSM) is an online mapping collaboration project [35]. Owing to continuous improvements by the public and the use of more reliable data sources, OSM provides higher accuracy and resolution in coastline data than GSHHG. Ultimately, we obtained coastline data for the SCS, totaling 2,547,051 points, for use as zero-depth estimates.

2.1.3. Multibeam Bathymetric Checking Data and ENC Data

Existing global seafloor topography model grid data can be retrieved and viewed using a Type Identifier Grid (TID). In this study, we extracted newly added multibeam data from the GEBCO2023 model, which are not included in the GEBCO2022 version, and used these as actual bathymetric checking points. These multibeam data additions have not yet been released in other global models. The 2,437,211 extracted multibeam bathymetric grid checkpoints served as external conformity verification data (denoted by red dots in Figure 2b).

Additionally, we selected two ENCs near the Zhongsha and Nansha Islands, identified by codes C13A7300 and C1318200. These charts comprise 3801 bathymetric points (denoted by black dots in Figure 2b) and were used as extra verification data to assess the accuracy of the seafloor topography models in nearshore and island areas [36]. The ENCs used in this study were obtained through Beijing Situo Ocean Information Technology Co., Ltd. (www.enclive.cn, accessed on 1 June 2024), authorized by the Chinese Naval Hydrographic Survey (https://www.msa.gov.cn/, accessed on 1 June 2024). The positions of the objects on the chart are based on the World Geodetic System 1984 (WGS-84). The scale is 1:250,000. All measured bathymetry data were obtained during 2023.

2.1.4. The Global Seafloor Topography Models

We utilized recently released seafloor topography models for comparison, including the SRTM15_V2.6 and the topo_V27.1 models published by SIO, the GEBCO_2022 model from the General Bathymetric Chart of the Oceans (GEBCO), and the SDUST2023BCO model developed by Shandong University of Science and Technology, which was trained with machine learning using global bathymetric data and multi-source geodetic data. We conducted accuracy comparisons of these models with the seafloor topography of the SCS derived from our method. Additionally, we assessed the PSD performance of various models at different wavelength bands based on different bathymetry data types and distribution densities. In the SCS, we further selected three typical areas: Area A, which has extensive single-beam coverage (112°E–118°E, 10°N–18°N); Area B, with limited bathymetric data coverage (110°E–114°E, 14°N–18°N); and Area C, which has more multibeam coverage (118°E–122°E, 19°N–22°N).

2.2. Methods

2.2.1. MGGM

The conventional GGM assumes that an observed gravity anomaly at a specific location can be decomposed into a long-wavelength gravity anomaly and a short-wavelength gravity anomaly. The long-wavelength gravity anomaly, g_{long}, is associated with more profound mass variations, such as variations in crustal thickness or large-scale geological features. The short-wavelength gravity anomaly, g_{short}, is linked to local bedrock variations. Accordingly, depth d can be decomposed into a long-wavelength (regional) component, d_{ref}, and a short-wavelength (residual) component, d_{res}, as follows:

$$g = g_{short} + g_{long} \tag{1}$$

$$d = d_{ref} + d_{res} \tag{2}$$

The seafloor topography inversion process uses the conventional GGM, incorporating depth constraints from control point data, and estimates the bathymetry based on g_{short} and relevant parameters.

However, the conventional GGM for constructing long-wavelength gravity anomalies primarily relies on interpolation at control points, which can introduce errors in areas lacking actual bathymetric data. Figure 3 illustrates the principle of the MGGM using depths along the profile of a depth grid. The MGGM accounts for the Bouguer term, a reference depth, a reference gravity field, and density contrast; this helps to construct long-wavelength results without relying on shipborne depth data [12].

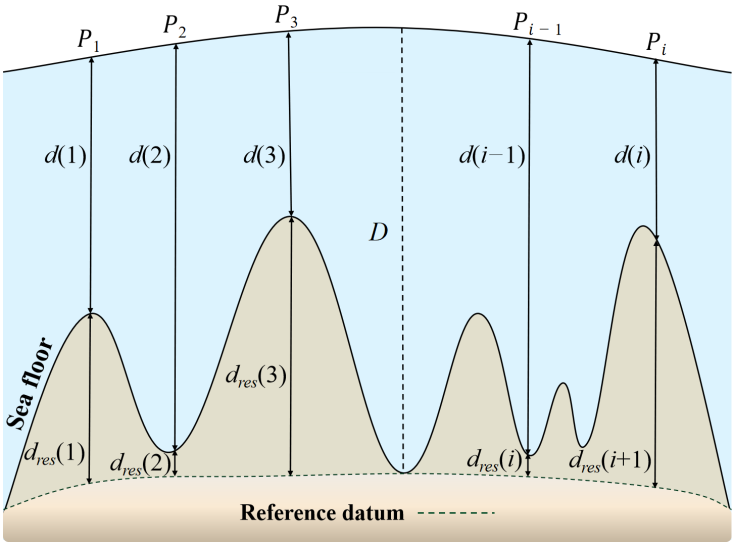


Figure 3. The principle of the MGGM.

In this study, smoothing the reference seafloor topography model, 'topo_V25.1', from SIO was performed using Gaussian filtering with a 10 km window width (referred to as topo25_GF10), and this result was used as d_{ref}. The first step uses d_{ref} to obtain the reference short-wavelength anomalies, $g_{short}(i)$:

$$g_{short}(i) = 2\pi G\Delta\rho(d_{ref}(i) - D) \tag{3}$$

in which G is the gravitational constant, 6.672×10^{-8} cm^3 g^{-1} s^{-2}, and $\Delta\rho$ is the difference in density between seawater and the ocean bottom rock. D represents the maximum depth within the reference model. Subsequently, long-wavelength gravity anomalies were obtained from the reference gravity field model (EGM2008):

$$g_{long}(i) = g_{ref}(i) - g_{short}(i) \tag{4}$$

In the second step, we removed $g_{long}(i)$ from the SDUST2022GRA model, $g(i)$, to obtain short-wavelength gravity, denoted by $g_{short}^{SDUST2022GRA}$:

$$g_{short}^{SDUST2022GRA}(i) = g(i) - g_{long}(i) \tag{5}$$

In the third step, we further refined and obtained the final results for the high-precision bathymetry, $d(i)$ (MGGM_BAT), by combining the results from the aforementioned formulas:

$$d(i) = \frac{g_{short}^{SDUST2022GRA}(i)}{2\pi G\Delta\rho} + d_{ref}(i) \tag{6}$$

In Equations (3) and (6), $\Delta\rho$ is calculated. This follows the process used in the conventional GGM to determine $\Delta\rho$. In this study, $\Delta\rho$ is determined through an iterative approach using regional depth control points. Specifically, we iteratively adjust the $\Delta\rho$ values at fixed intervals, calculating the corresponding MGGM-derived bathymetric models for each value. Depth values from the bathymetric model are then interpolated and compared with shipborne depth data. The $\Delta\rho$ value that yields the best accuracy is considered the optimal value for this study, though it holds no physical significance and serves only as a numerical reference [13,14]. A $\Delta\rho$ of 8.7 cm^3 g^{-1} was used during the seafloor topography inversion process in this study.

2.2.2. BPNN

An FC-DNN can map multiple input variables through nonlinear transformations to generate one or more output variables [37,38]. BPNN is a type of FC-DNN trained using a backpropagation algorithm, which enables neurons to execute complex nonlinear mapping between input models and output data [39]. BPNN offers significant improvements by utilizing shipborne depth data to restore short-wavelength bathymetric information based on the depth model constructed by the MGGM, as well as by capturing nonlinear relationships that the MGGM cannot model owing to its reliance on linear assumptions.

Figure 4 illustrates the key steps used to obtain the BPGGM_BAT model by retraining with various types of data introduced in Section 2.1. The data preprocessing stage involves inputting datasets, including the SDUST2022GRA model, the EGM2008 model, the MGGM_BAT model, the topo25_GF10 model, and the topo_V25.1 model. Spatial location information such as longitude and latitude, crucial for model accuracy, along with other datasets, serves as the input. The outputs are shipborne depth data and coastline data used as zero-depth estimates, as shown in Figure 2a, ensuring one-to-one correspondence between inputs and outputs. The training, validation, and testing of the BPNN are conducted in an 8:1:1 ratio. To enhance the network's efficiency and stability while preventing issues like gradient explosions or vanishing, the input and output data need to be standardized. The network's complexity is managed through the number of hidden layers and their neuron counts. More hidden layers or neurons can improve learning capabilities but may cause overfitting, especially with limited data. Conversely, fewer layers or neurons might lead to underfitting, hindering the network's ability to learn data patterns effectively. The final network configuration consists of five hidden layers with neuron counts of 10, 15, 10, 15, and 5. For the neurons in the layer, l, their output, $a^{(l)}$, is calculated using the following formulas. First, the neurons receive the activation output from the previous layer, $a^{(l-1)}$, and perform a linear combination with the weight matrix $W^{(l)}$ and the bias term $b^{(l)}$, resulting in linear combination $z^{(l)}$, expressed as

$$z^{(l)} = W^{(l)} a^{(l-1)} + b^{(l)} \tag{7}$$

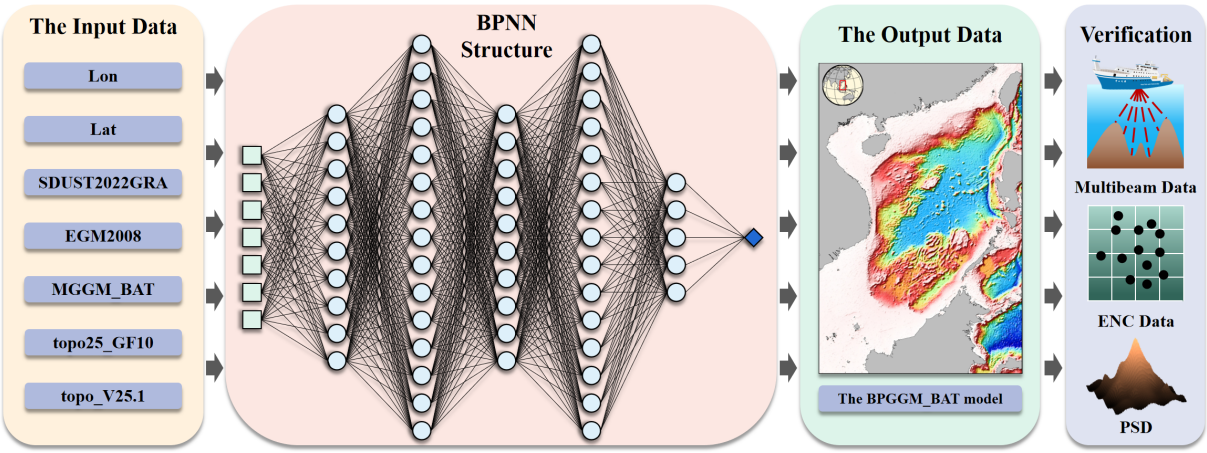


Figure 4. BPGGM_BAT seafloor topography model construction process and BPNN structure.

Next, the linear combination result, $z^{(l)}$, is passed through a nonlinear activation function, $f(z)$, to compute the final output of the layer, l:

$$a^{(l)} = f(z^{(l)}) \tag{8}$$

The activation function, $f(z)$, can be a nonlinear function, such as a sigmoid, relu, or tansig, which allows for the network to capture complex, nonlinear relationships [40]. The hidden layers utilize the tansig activation function, the mathematical expression for which is

$$f(z) = \frac{2}{1 + e^{-2z}} - 1 \tag{9}$$

This nonlinearity enhances the model's ability to capture more intricate patterns in the data, while the output layer utilizes the purelin activation function to maintain a linear relationship for continuous output. The network is trained for 1000 iterations to improve prediction accuracy by minimizing the loss function. A commonly used loss function is the mean squared error (MSE), denoted by L, which measures the difference between the predicted output and the actual output. The formula for L is as follows:

$$L = \frac{1}{m} \sum_{i=1}^{m} (\hat{y}^{(i)} - y^{(i)})^2 \tag{10}$$

where m is the number of samples, $\hat{y}^{(i)}$ is the predicted value of the network, and $y^{(i)}$ is the actual depth data from our research. Through the backpropagation algorithm, the network computes the gradient of the loss function with respect to the weights and biases layer by layer. These gradients are then used to update the weights and biases via the Levenberg–Marquardt method [41]. The weight and bias update rule is specified in the following equation:

$$W^{(l)*} = W^{(l)} - \alpha \frac{\partial L}{\partial W^{(l)}} \tag{11}$$

$$b^{(l)*} = b^{(l)} - \alpha \frac{\partial L}{\partial b^{(l)}} \tag{12}$$

where $W^{(l)*}$ denotes the updated weights, $b^{(l)*}$ denotes the updated biases, and α represents the learning rate, which is set to 0.01 in this study and signifies the step length taken along the gradient direction. Through continuous iterative updates, the network gradually converges, the error decreases, and the model is eventually optimized. After the training is completed, the model grid data in the SCS region are input into the network to build the final BPGGM_BAT model. The accuracy of this model is then evaluated to confirm its suitability, as shown in Figure 4.

3. Results and Discussion

3.1. Inversion Results

Figure 5 shows the seafloor topography of the MGGM_BAT and BPGGM_BAT models, along with their differences in the SCS. Both models effectively reflect significant and complex variations in seafloor topography. From the coastal areas to the central basin, the seafloor topography descends in a stepwise manner, with depths gradually reaching over 5000 m at the basin center. The seafloor topography comprises the shelf, the slope, and deep-sea basin geomorphological units, with generally flat deep-sea basins that also feature numerous seamounts and knolls. On the one hand, the main differences between the two models are concentrated in nearshore and island areas, such as around the Dongsha, Xisha, Zhongsha, and Nansha Islands. This outcome may be due to the coastline being used as the zero-depth reference, improving seafloor topography estimation in these regions. On the other hand, differences are primarily located in complex terrains, such as the seamounts in the central basin and the Manila Trench, likely because of the BPNN's ability to capture bathymetric signals. Additional bathymetric validation data are required to further verify the models' accuracy.

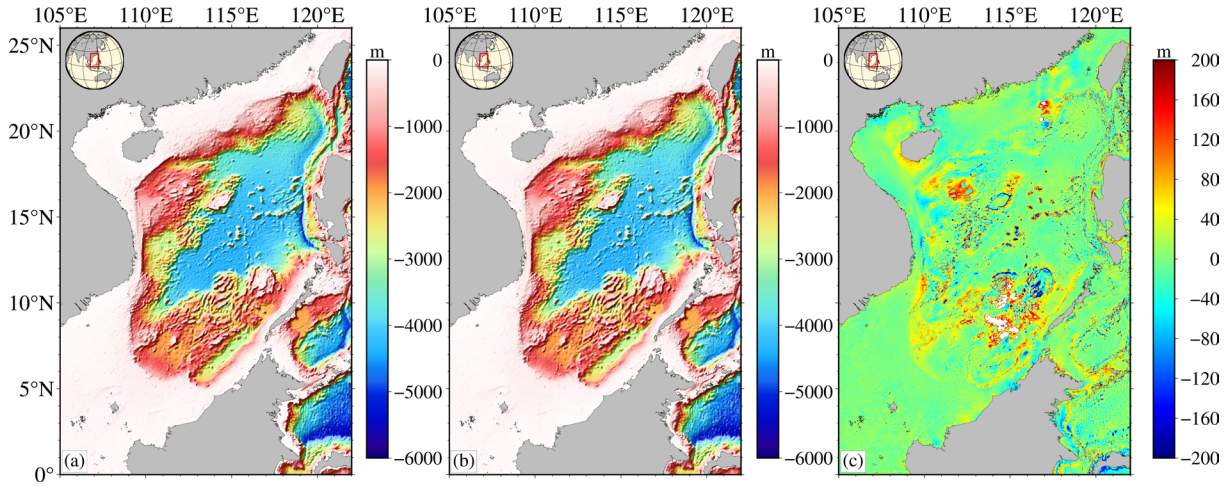


Figure 5. Seafloor topography models: (**a**) the MGGM_BAT model; (**b**) the BPGGM_BAT model; (**c**) differences between the MGGM_BAT model and the BPGGM_BAT model.

3.2. Evaluation of Seafloor Topography Models' Accuracy

3.2.1. Comparison with Multibeam Data

In this section, we evaluate the MGGM_BAT model, the BPGGM_BAT model, and other recently released models using multibeam bathymetric data. The differences between these seafloor topography models and the multibeam sounding verification data can be primarily observed in two regions (Figure 6). The first region with significant errors includes the areas around the Nansha Islands, the Zhongsha Islands, and the nearshore areas of the continental slopes that extend from the periphery toward the center of the central basin. The second region, where errors are primarily located, includes more complex topography changes such as seamounts, sea tables, troughs, ridges, valleys, and submarine fans in the southeastern archipelago. In these areas, the precision of the gravity anomaly models is lower, actual bathymetric data are sparse, and the seafloor topography is significantly undulated, leading to larger discrepancies between the inverted seafloor topography models and the multibeam sounding data. Additionally, the $\Delta\rho$ values used in Equations (3) and (6) are derived from bathymetric data covering the SCS area. The estimated $\Delta\rho$ is variable across different depth ranges, especially in nearshore areas, leading to lower model accuracy in these regions.

Visually, the spatial distribution of deviations between these models and multibeam bathymetric data is not significantly different. Table 1 presents the results of further statistical analysis of these differences, with R representing the correlation coefficient between the seafloor topography models and the multibeam data. The BPGGM_BAT model achieves optimal precision in its deviations with multibeam data, with a correlation coefficient reaching 0.993, consistent with the SDUST2023BCO model. Compared with the MGGM_BAT model, the BPGGM_BAT model decreases the RMS of differences with multibeam data from 154.33 m to 140.43 m. The BPGGM_BAT model reduces the RMS and STD of differences by up to 8–9% compared with the MGGM_BAT in the SCS. Compared with the recently released SRTM15_V2.6, GEBCO_2022, and topo_V27.1 models, the BPGGM_BAT model can reduce the RMS of deviations with multibeam data by 24.3 m, 35.33 m, and 34.1 m, respectively, and the STD results by 31.32 m, 32.5 m, and 31.4 m. Compared with the topo_V25.1 and topo25_GF10 models used as training data, the BPGGM_BAT model shows reductions in RMS deviations with multibeam data by 18.95 m and 25.72 m, respectively, and reductions in STD by 17.27 m and 24.14 m. The accuracy of the BPGGM_BAT model improves by approximately 18% to 20% relative to these models, and it is comparable to that of the SDUST2023BCO model. Additionally, the maximum, minimum, and mean differences in the BPGGM_BAT model with multibeam data are the best among all the models.

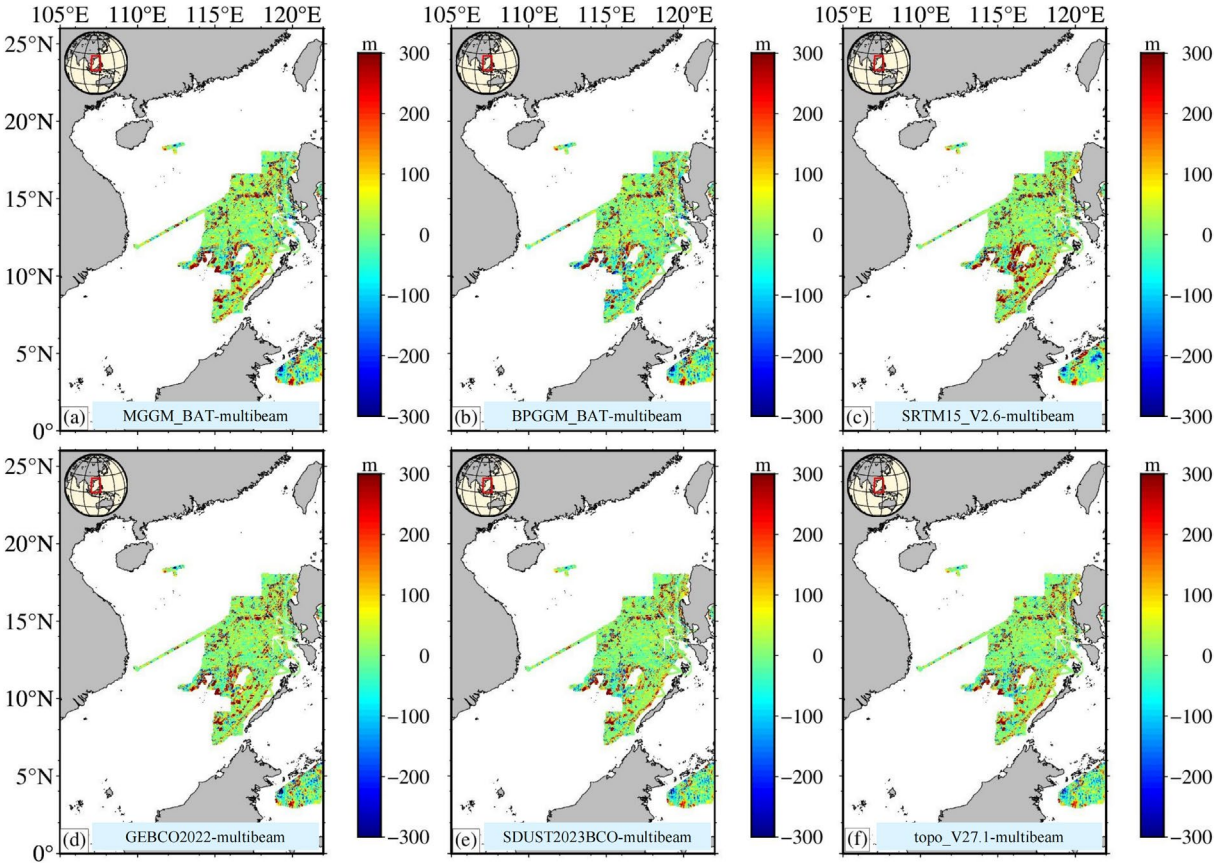


Figure 6. Spatial distribution of the differences between the seafloor topography models and multibeam depth data: (**a**) between MGGM_BAT model and multibeam data; (**b**–**f**) same as (**a**) but for BPGGM_BAT, SRTM15 V2.6, GEBCO2022, SDUST2023BCO, and topo_V27.1, respectively.

Table 1. Statistics for the differences and correlation between models and multibeam data.

Model	Max/m	Min/m	Mean/m	RMS/m	STD/m	R
MGGM_BAT	2008.15	−1703.01	27.62	154.33	151.84	0.992
BPGGM_BAT	1801.53	−1509.50	14.51	140.43	139.68	0.993
SRTM15_V2.6	2416.36	−2096.19	35.90	174.73	171.00	0.991
GEBCO_2022	3997.00	−2353.00	35.31	175.76	172.18	0.990
SDUST2023BCO	2288.94	−2410.43	22.50	143.58	141.80	0.993
topo_V27.1	2502.70	−2107.61	34.52	174.53	171.08	0.991
topo_V25.1	2244.54	−1656.88	27.69	159.38	156.95	0.992
topo25_GF10	2473.09	−2198.33	27.69	166.15	163.82	0.991

Figure 7 displays frequency distributions of the differences between seafloor topography models and multibeam data. The range of deviations between the models and multibeam data primarily falls within [−300, 300]. The BPGGM_BAT and SDUST2023BCO models show the best proportion of differences with multibeam data within a range of [−200, 200], with proportions of 89.7% and 90.79%, respectively. The SRTM15_V2.6 and topo_V27.1 models display similar accuracy and frequency distributions with the multibeam data, likely because the SRTM15_V2.6 model is based on the topo_V27.1 model and is produced as a 15″ resolution seafloor topography model. A statistical analysis of deviations between the models and the multibeam data revealed more positive than negative differences, indicating that all models tend to underestimate bathymetry. On the one hand, lower-density sediments may accumulate around seamounts, resulting in weaker local gravity anomalies and, consequently, shallower inferred bathymetry. On the other hand, in nearshore areas such as continental shelves and slopes, sediments often have lower densi-

ties than surrounding bedrock. Sediment cover can weaken or complicate gravity anomaly signals, thus reducing the correlation between bathymetry and gravitational anomalies. As a result, the main discrepancies can be observed around seamounts and in nearshore areas (Figure 6).

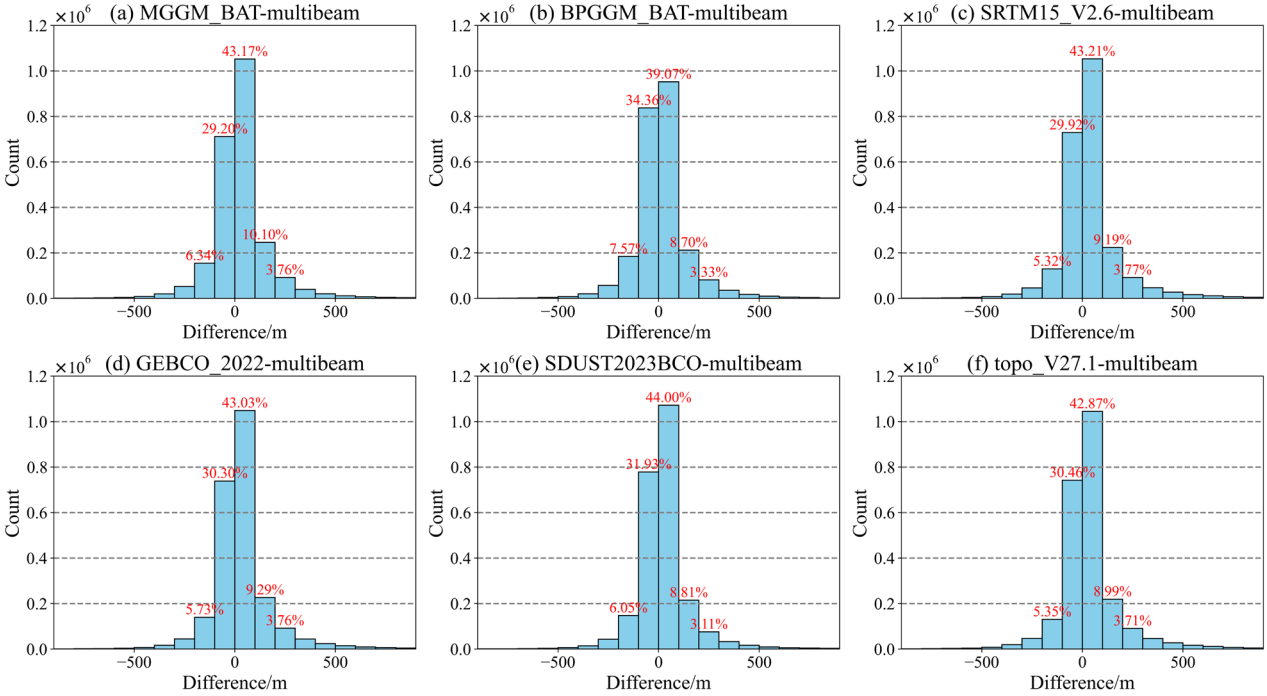


Figure 7. Frequency distribution of the differences between models and multibeam data: (**a**) between MGGM_BAT model and multibeam data; (**b**–**f**) same as (**a**) but for BPGGM_BAT, SRTM15 V2.6, GEBCO2022, SDUST2023BCO, and topo_V27.1, respectively.

3.2.2. Comparison with ENC Verification Data

In addition, we conducted precision assessments of various models using bathymetric chart points in regions near the Zhongsha and Nansha Islands (Table 2). Compared with the results in Table 1, which assessed model accuracy based on multibeam data, the precision statistics for differences between the chart depths and models in Table 2 are generally consistent, except for the GEBCO2022 model. The BPGGM_BAT model displayed the best accuracy among the assessment results. Compared with those for the MGGM_BAT model, the maximum, minimum, mean, RMS, and STD of differences between the BPGGM_BAT model and the chart depths decreased by 126.86 m, −159.09 m, −33.14 m, 34.39 m, and 27.78 m, respectively, indicating improvements in all precision parameters. Compared with those for the recently released SRTM15_V2.6, GEBCO_2022, SDUST2023BCO, and topo_V27.1 global seafloor topography models, the RMS of the BPGGM_BAT model's deviations relative to the chart depths improved by 65.05 m, 12.57 m, 24.15 m, and 65.34 m, and the STD improved by 63.6 m, 13.54 m, 25.17 m, and 64.09 m, respectively. Compared with the topo_V25.1 and topo25_GF10 models used as input data for BPNN training, the final BPGGM_BAT model demonstrates a significant improvement in accuracy. According to these evaluation results, the relative accuracy of the model can improve by 8% to 33% relative to these six models. The correlation coefficients between all seafloor topography models and the chart depths exceed 0.98, with the BPGGM_BAT model still achieving the highest correlation coefficient consistently at 0.993, as shown in Table 1. The ENC depth data are concentrated around the nearshore islands and reefs, as shown in Figure 2b. The GEBCO2022 model supplements chart data in nearshore areas such as coastlines and continental slopes, relying not solely on gravity-derived bathymetric results, leading to superior accuracy in these regions.

Table 2. Statistics for the differences and correlation between models and ENC bathymetric data.

Model	Max/m	Min/m	Mean/m	RMS/m	STD/m	R
MGGM_BAT	866.15	−1043.72	−50.57	169.09	161.37	0.990
BPGGM_BAT	739.29	−884.63	−17.43	134.70	133.59	0.993
SRTM15_V2.6	1894.73	−989.66	32.07	199.75	197.19	0.985
GEBCO_2022	1916.53	−724.15	6.90	147.27	147.13	0.991
SDUST2023BCO	1206.97	−962.72	−5.85	158.85	158.76	0.990
topo_V27.1	1868.86	−990.23	30.82	200.04	197.68	0.984
topo_V25.1	991.05	−981.92	−39.88	162.19	157.23	0.990
topo25_GF10	876.11	−1087.92	−52.15	174.01	166.04	0.989

Figure 8 shows frequency histograms of the differences between various seafloor topography models and ENC depth data, with most differences concentrated within a range of [−200, 200]. Compared with the MGGM_BAT model, the BPGGM_BAT model shows a significant 10.9% reduction in the range of depths where the absolute difference exceeds 100 m. The SRTM15_V2.6 and topo_V27.1 models exhibit differences primarily concentrated in the [−100, 100] range, with an essentially identical frequency distribution of depth differences between these two models. In the range of differences within [−200, 200], the proportions for the MGGM_BAT, BPGGM_BAT, SRTM15_V2.6, GEBCO_2022, SDUST2023BCO, and topo_V27.1 models are 82.76%, 89.37%, 86.08%, 90.12%, 84.90%, and 85.93%, respectively. Overall, the BPGGM_BAT model outperforms the MGGM_BAT and SDUST2023BCO models in terms of deviations relative to the chart data, and its frequency distribution closely aligns with the GEBCO_2022 model.

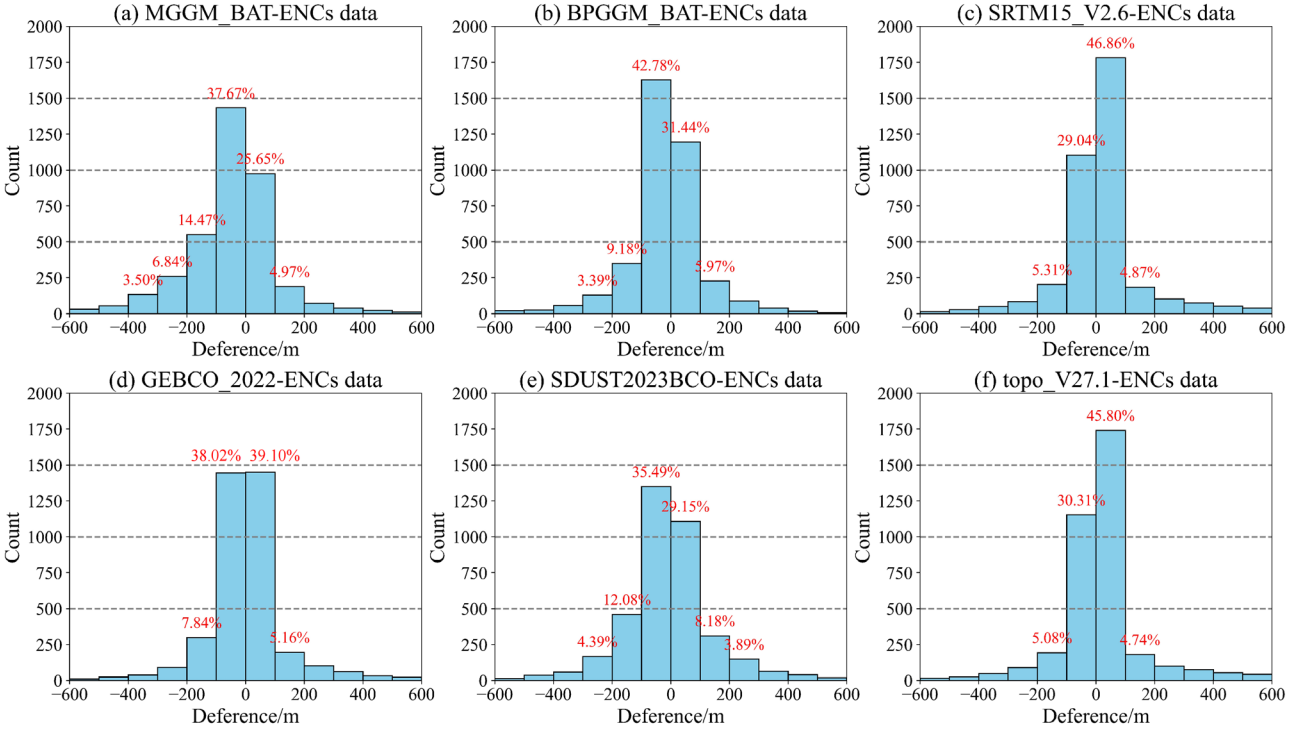


Figure 8. Frequency distribution of differences between models and ENC bathymetric data: (**a**) between MGGM_BAT model and ENC bathymetric data; (**b**–**f**) same as (**a**) but for BPGGM_BAT, SRTM15 V2.6, GEBCO2022, SDUST2023BCO, and topo_V27.1, respectively.

3.3. Power Spectral Density Analysis of Models

To further assess the performance of various seafloor topography models in different spatial scales, we calculate the PSD in the radial direction using the "grdfft" module in GMT. Figure 9 depicts the PSD amplitudes for the BPGGM_BAT and MGGM_BAT models.

For comparison, Figure 9 also includes the PSD of the SDUST2023BCO and topo_V27.1 models with a 1′ resolution. In general, larger PSD values indicate that larger variations in seafloor topography have been effectively captured, and they are commonly utilized as supplementary indicators to assess the performance of bathymetry reconstruction methods [24]. Over short wavelengths (less than 15 km), the BPGGM_BAT model performs better than the MGGM_BAT model, showing stronger power in these three areas. Therefore, the PSD results appear to indicate that the BPGGM_BAT model effectively recovers more variable bathymetry at a small scale than the MGGM_BAT model. Additionally, in regions A and C, where bathymetric information is relatively abundant, the BPGGM_BAT model performs slightly better than the SDUST2023BCO and topo_V27.1 models in the shorter wavelength. The poor performance of the SDUST2023BCO model in Area C may be due to a lack of supplementary multibeam data for model construction. Applying high-precision gravity anomaly information and prior actual bathymetric data helps to further enhance the quality of the seafloor topography model obtained via the MGGM.

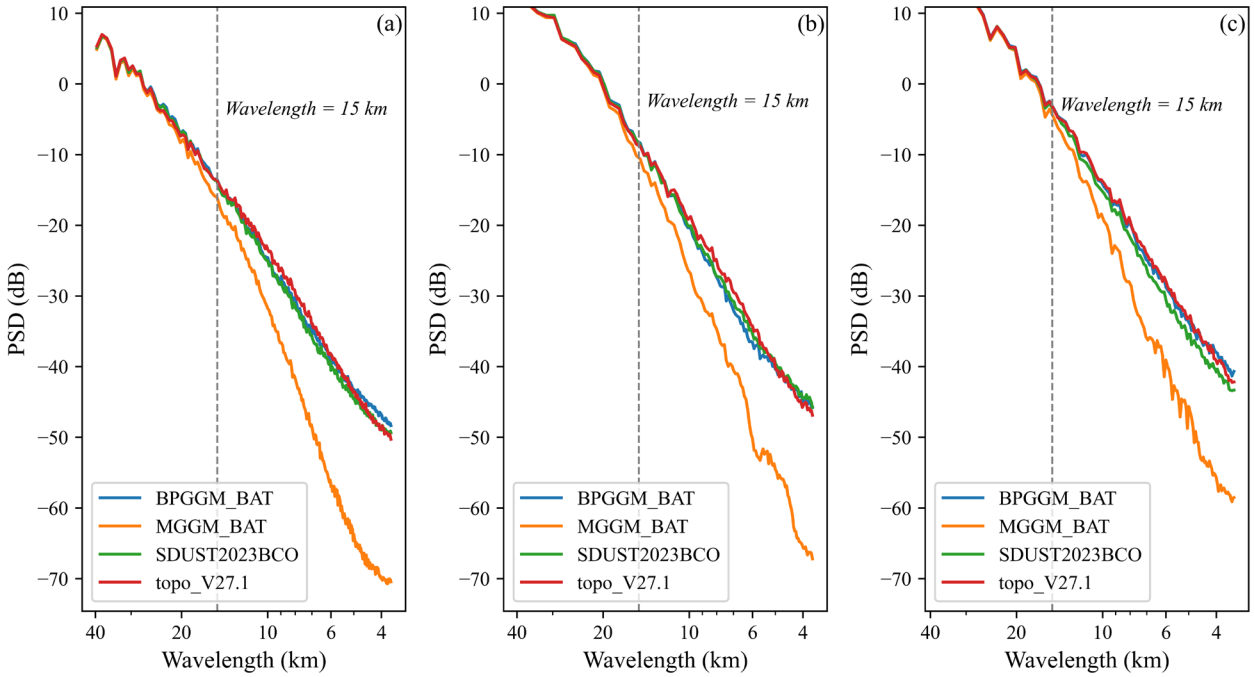


Figure 9. Power spectral densities of bathymetry models in the radial direction. (**a**) Area A, which has extensive single-beam data coverage (112°E–118°E, 10°N–18°N). (**b**) Area B, which has limited bathymetric data coverage (110°E–114°E, 14°N–18°N). (**c**) Area C, which has extensive multibeam data coverage (118°E–122°E, 19°N–22°N).

4. Conclusions

To improve the precision of seafloor topography models in the SCS, we used a BPNN combined with the MGGM, incorporating the SDUST2022GRA gravity anomaly model, shipborne depth soundings, and coastline data as zero-depth estimates to construct a bathymetric model (BPGGM_BAT) of the region. According to the precision assessment results, the BPGGM_BAT model is more consistent with the multibeam data than the other models, achieving an optimal correlation coefficient of 0.993. Relative to the multibeam verification data, the RMS of differences in the BPGGM_BAT model decreased from 154.33 m to 140.43 m, and the STD decreased from 151.84 m to 139.68 m compared with the MGGM_BAT model. In addition, the BPGGM_BAT model's precision is approximately 18% to 20% higher than that of the SRTM15_V2.6, GEBCO_2022, and topo_V27.1 models and is comparable to that of the SDUST2023BCO model.

To further evaluate the model's performance in shallow nearshore areas, such as around islands and reefs, we used ENC bathymetric data from regions near the Zhongsha and Nansha Islands as an additional means to assess model accuracy. According to the frequency distribution of differences between the model depths and chart depths, the BPGGM_BAT model demonstrated a more significant reduction in absolute depth differences exceeding 100 m than the MGGM_BAT model. The difference RMS between the BPGGM_BAT model and the ENC depths decreased by 34.39 m, 65.05 m, 12.57 m, 24.15 m, and 65.34 m compared with the MGGM_BAT, SRTM15_V2.6, GEBCO_2022, SDUST2023BCO, and topo_V27.1 models, and the STD decreased by 27.78 m, 63.6 m, 13.54 m, 25.17 m, and 64.09 m, respectively. Consequently, the relative accuracy of the BPGGM_BAT model improved by 8% to 33% compared with those models. The PSD analysis indicates that the BPGGM_BAT model exhibits superior performance at scales less than 15 km compared with the MGGM_BAT model.

The evaluation using various types of bathymetric verification data consistently demonstrated the high quality of the BPGGM_BAT model. The combination of MGGM and BPNN offers a new approach to seafloor topography inversion based on satellite altimetry-derived gravity data, with the potential for global implementation. Beyond algorithmic combination improvements, applying high-precision gravity anomaly data and extensive bathymetric information plays a crucial role in constructing accurate seafloor topography models. During the construction of the SCS seafloor topography model, certain inaccuracies may exist in nearshore areas such as coastlines and islands owing to the limited use of available depth data. To overcome these limitations and enhance the accuracy of seafloor topography in shallow and coastal regions, recently available depth data should be incorporated, such as airborne bathymetric LiDAR data [42] and satellite-derived bathymetric (SDB) data [43]. Furthermore, the new generation of altimetry satellites, such as SWOT, is expected to provide more refined gravity information [44,45], thereby enabling the feasible creation of higher-quality seafloor topography models.

Author Contributions: X.C. and M.Z.—original draft preparation; X.C. and M.Z.—conceptualization; W.F., M.Y., and M.Z.—supervision; X.C., M.Y., M.S., D.A., and W.F.—review and editing. All authors have read and agreed to the published version of the manuscript.

Funding: This research was funded by the National Natural Science Foundation of China (Grant no. 42027802); the open fund of key laboratory (Grant no. MESTA-2022-B003); the Fundamental Research Funds for the Central Universities, Sun Yat-sen University (Grant nos. 23xkjc012, 24xkjc027).

Data Availability Statement: The MGGM_BAT and BPGGM_BAT seafloor topography models in the South China Sea are available at https://zenodo.org/records/13861508 (accessed on 30 September 2024).

Acknowledgments: We would like to express our gratitude to several institutions for their contributions to our work. Shandong University of Science and Technology provided the SDUST2022GRA global marine gravity anomalies (https://zenodo.org/records/8337387, accessed on 1 August 2024) and the SDUST2023BCO global seafloor topography model (https://zenodo.org/records/13341896, accessed on 1 August 2024). The International Centre for Global Earth Models (ICGEM) supplied the EGM2008 gravity anomaly results (https://icgem.gfz-potsdam.de/home, accessed on 1 August 2024). We are also grateful to the Scripps Institution of Oceanography for the topo_V25.1, topo_V27.1, and SRTM15_V2.6 models (https://topex.ucsd.edu/pub/, accessed on 1 August 2024), and to the General Bathymetric Chart of the Oceans organization for the GEBCO_2022 and GEBCO_2023 models (https://www.gebco.net/data_and_products/gridded_bathymetry_data/, accessed on 1 August 2024). Additionally, we thank the National Centers for Environmental Information (NCEI) for providing shipboard bathymetry (https://www.ncei.noaa.gov/maps/geophysics/, accessed on 1 August 2024), OpenStreetMap (OSM) for providing coastline data (https://osmdata.openstreetmap.de/data/coast.html, accessed on 1 August 2024), and the anonymous reviewers for their valuable feedback that substantially improved this work.

Conflicts of Interest: The authors declare no conflicts of interest.

References

1. Hwang, C.; Chang, E.T. Seafloor secrets revealed. *Science* **2014**, *346*, 32–33. [CrossRef] [PubMed]
2. DeSanto, J.B.; Sandwell, D.T. Meter-scale seafloor geodetic measurements obtained from repeated multibeam sidescan surveys. *Mar. Geod.* **2019**, *42*, 491–506. [CrossRef]
3. Smith, W.H.; Sandwell, D.T. Bathymetric prediction from dense satellite altimetry and sparse shipboard bathymetry. *J. Geophys. Res. Solid Earth* **1994**, *99*, 21803–21824. [CrossRef]
4. Sandwell, D.T.; Smith, W.H. Marine gravity anomaly from Geosat and ERS 1 satellite altimetry. *J. Geophys. Res. Solid Earth* **1997**, *102*, 10039–10054. [CrossRef]
5. Mayer, L.; Jakobsson, M.; Allen, G.; Dorschel, B.; Falconer, R.; Ferrini, V.; Lamarche, G.; Snaith, H.; Weatherall, P. The Nippon Foundation—GEBCO seabed 2030 project: The quest to see the world's oceans completely mapped by 2030. *Geosciences* **2018**, *8*, 63. [CrossRef]
6. Tozer, B.; Sandwell, D.T.; Smith, W.H.; Olson, C.; Beale, J.; Wessel, P. Global bathymetry and topography at 15 arc sec: SRTM15+. *Earth Space Sci.* **2019**, *6*, 1847–1864. [CrossRef]
7. Hu, M.; Li, L.; Jin, T.; Jiang, W.; Wen, H.; Li, J. A New $1' \times 1'$ Global Seafloor Topography Model Predicted from Satellite Altimetric Vertical Gravity Gradient Anomaly and Ship Soundings BAT_VGG2021. *Remote Sens.* **2021**, *13*, 3515. [CrossRef]
8. An, D.; Guo, J.; Chang, X.; Wang, Z.; Jia, Y.; Liu, X.; Bondur, V.; Sun, H. High-precision $1' \times 1'$ bathymetric model of Philippine Sea inversed from marine gravity anomalies. *EGUsphere* **2023**, *2023*, 1–23. [CrossRef]
9. Smith, W.H.; Sandwell, D.T. Global sea floor topography from satellite altimetry and ship depth soundings. *Science* **1997**, *277*, 1956–1962. [CrossRef]
10. Xu, C.; Li, J.; Jian, G.; Wu, Y.; Zhang, Y. An adaptive nonlinear iterative method for predicting seafloor topography from altimetry-derived gravity data. *J. Geophys. Res. Solid Earth* **2023**, *128*, e2022JB025692. [CrossRef]
11. Kim, J.W.; von Frese, R.R.; Lee, B.Y.; Roman, D.R.; Doh, S.-J. Altimetry-derived gravity predictions of bathymetry by the gravity-geologic method. *Pure Appl. Geophys.* **2011**, *168*, 815–826. [CrossRef]
12. Hsiao, Y.-S.; Hwang, C.; Cheng, Y.-S.; Chen, L.-C.; Hsu, H.-J.; Tsai, J.-H.; Liu, C.-L.; Wang, C.-C.; Liu, Y.-C.; Kao, Y.-C. High-resolution depth and coastline over major atolls of South China Sea from satellite altimetry and imagery. *Remote Sens. Environ.* **2016**, *176*, 69–83. [CrossRef]
13. Wei, Z.; Guo, J.; Zhu, C.; Yuan, J.; Chang, X.; Ji, B. Evaluating Accuracy of HY-2A/GM-Derived Gravity Data with the Gravity-Geologic Method to Predict Bathymetry. *Front. Earth Sci.* **2021**, *9*, 636246. [CrossRef]
14. An, D.; Guo, J.; Li, Z.; Ji, B.; Liu, X.; Chang, X. Improved Gravity-Geologic Method Reliably Removing the Long-Wavelength Gravity Effect of Regional Seafloor Topography: A Case of Bathymetric Prediction in the South China Sea. *IEEE Trans. Geosci. Remote Sens.* **2022**, *60*, 4211912. [CrossRef]
15. Jiang, X.; Guo, J.; Lin, M.; Sun, H.; Jiang, T. Enhanced gravity-geologic method to predict bathymetry by considering non-linear effects of surrounding seafloor topography. *Geophys. J. Int.* **2024**, *239*, 754–767. [CrossRef]
16. Fan, D.; Li, S.; Li, X.; Yang, J.; Wan, X. Seafloor topography estimation from gravity anomaly and vertical gravity gradient using nonlinear iterative least square method. *Remote Sens.* **2020**, *13*, 64. [CrossRef]
17. Annan, R.F.; Wan, X. Recovering Bathymetry of the Gulf of Guinea Using Altimetry-Derived Gravity Field Products Combined via Convolutional Neural Network. *Surv. Geophys.* **2022**, *43*, 1541–1561. [CrossRef]
18. Wan, X.; Annan, R.F.; Ziggah, Y.Y. Altimetry-Derived Gravity Gradients Using Spectral Method and Their Performance in Bathymetry Inversion Using Back-Propagation Neural Network. *J. Geophys. Res. Solid Earth* **2023**, *128*, e2022JB025785. [CrossRef]
19. Harper, H.; Sandwell, D.T. Global predicted bathymetry using neural networks. *Earth Space Sci.* **2024**, *11*, e2023EA003199. [CrossRef]
20. Xing, J.; Chen, X.-X.; Ma, L. Bathymetry inversion using the modified gravity-geologic method: Application of the rectangular prism model and Tikhonov regularization. *Appl. Geophys.* **2020**, *17*, 377–389. [CrossRef]
21. Zhou, S.; Liu, X.; Guo, J.; Jin, X.; Yang, L.; Sun, Y.; Sun, H. Bathymetry of the Gulf of Mexico predicted with multilayer perceptron from multi-source marine geodetic data. *IEEE Trans. Geosci. Remote Sens.* **2023**, *61*, 4208911. [CrossRef]
22. Zhou, S.; Liu, X.; Sun, Y.; Chang, X.; Jia, Y.; Guo, J.; Sun, H. Predicting bathymetry using multisource differential marine geodetic data with multilayer perceptron neural network. *Int. J. Digit. Earth* **2024**, *17*, 2393255. [CrossRef]
23. Sun, H.; Feng, Y.; Fu, Y.; Sun, W.; Peng, C.; Zhou, X.; Zhou, D. Bathymetric prediction using multisource gravity data derived from a parallel linked BP neural network. *J. Geophys. Res. Solid Earth* **2022**, *127*, e2022JB024428. [CrossRef]
24. Yang, L.; Liu, M.; Liu, N.; Guo, J.; Lin, L.; Zhang, Y.; Du, X.; Xu, Y.; Zhu, C.; Wang, Y. Recovering Bathymetry from Satellite Altimetry-derived Gravity by Fully Connected Deep Neural Network. *IEEE Geosci. Remote Sens. Lett.* **2023**, *20*, 1502805. [CrossRef]
25. Sandwell, D.T.; Müller, R.D.; Smith, W.H.; Garcia, E.; Francis, R. New global marine gravity model from CryoSat-2 and Jason-1 reveals buried tectonic structure. *Science* **2014**, *346*, 65–67. [CrossRef]
26. Andersen, O.B.; Knudsen, P. The DTU17 global marine gravity field: First validation results. In *Fiducial Reference Measurements for Altimetry, International Association of Geodesy Symposia*; Mertikas, S., Pail, R., Eds.; Springer: Berlin/Heidelberg, Germany, 2019; Volume 150, pp. 83–87.
27. Zhang, S.; Zhou, R.; Jia, Y.; Jin, T.; Kong, X. Performance of HaiYang-2 Altimetric Data in Marine Gravity Research and a New Global Marine Gravity Model NSOAS22. *Remote Sens.* **2022**, *14*, 4322. [CrossRef]

28. Zhu, C.; Guo, J.; Hwang, C.; Gao, J.; Yuan, J.; Liu, X. How HY-2A/GM altimeter performs in marine gravity derivation: Assessment in the South China Sea. *Geophys. J. Int.* **2019**, *219*, 1056–1064.
29. Zhu, C.; Guo, J.; Yuan, J.; Li, Z.; Liu, X.; Gao, J. SDUST2021GRA: Global marine gravity anomaly model recovered from Ka-band and Ku-band satellite altimeter data. *Earth Syst. Sci. Data* **2022**, *14*, 4589–4606. [CrossRef]
30. Li, Z.; Guo, J.; Zhu, C.; Liu, X.; Hwang, C.; Lebedev, S.; Chang, X.; Soloviev, A.; Sun, H. The SDUST2022GRA global marine gravity anomalies recovered from radar and laser altimeter data: Contribution of ICESat-2 laser altimetry. *Earth Syst. Sci. Data* **2024**, *16*, 4119–4135. [CrossRef]
31. Wan, X.; Wang, H.; Jia, Y.; Ma, W. Performance of Haiyang-2 derived gravity field products in bathymetry inversion. *Remote Sens.* **2022**, *15*, 32. [CrossRef]
32. Zhou, S.; Guo, J.; Zhang, H.; Jia, Y.; Sun, H.; Liu, X.; An, D. SDUST2023BCO: A global seafloor model determined from multi-layer perceptron neural network using multi-source differential marine geodetic data. *Earth Syst. Sci. Data* **2024**. submitted.
33. Li, Z.; Guo, J.; Ji, B.; Wan, X.; Zhang, S. A Review of Marine Gravity Field Recovery from Satellite Altimetry. *Remote Sens.* **2022**, *14*, 4790. [CrossRef]
34. Wessel, P.; Luis, J.; Uieda, L.; Scharroo, R.; Wobbe, F.; Smith, W.H.; Tian, D. The generic mapping tools version 6. *Geochem. Geophys. Geosystems* **2019**, *20*, 5556–5564. [CrossRef]
35. Goodchild, M.F. Citizens as sensors: The world of volunteered geography. *GeoJournal* **2007**, *69*, 211–221. [CrossRef]
36. Ruan, X.G.; Cheng, L.; Chu, S.S.; Yan, Z.J.; Zhou, X.; Duan, Z.X.; Li, M.C. A new digital bathymetric model of the South China Sea based on the subregional fusion of seven global sea floor topography products. *Geomorphology* **2020**, *370*, 107403. [CrossRef]
37. Hinton, G.E.; Salakhutdinov, R.R. Reducing the dimensionality of data with neural networks. *Science* **2006**, *313*, 504–507. [CrossRef]
38. Zhang, B.; Yang, M.; Feng, W.; Jiang, M.; Yan, X.; Zhong, M. RTM Gravity Forward Modelling using Improved Fully Connected Deep Neural Networks. *IEEE Trans. Geosci. Remote Sens.* **2024**, *62*, 5926911.
39. Karsoliya, S. Approximating number of hidden layer neurons in multiple hidden layer BPNN architecture. *Int. J. Eng. Trends Technol.* **2012**, *3*, 714–717.
40. Dubey, S.R.; Singh, S.K.; Chaudhuri, B.B. Activation functions in deep learning: A comprehensive survey and benchmark. *Neurocomputing* **2022**, *503*, 92–108.
41. Moré, J.J. The Levenberg-Marquardt algorithm: Implementation and theory. In *Numerical Analysis: Proceedings of the Biennial Conference Held at Dundee, 28 June–1 July 1977*; Springer: Berlin/Heidelberg, Germany, 2006.
42. Ma, Y.; Xu, N.; Liu, Z.; Yang, B.; Yang, F.; Wang, X.H.; Li, S. Satellite-derived bathymetry using the ICESat-2 lidar and Sentinel-2 imagery datasets. *Remote Sens. Environ.* **2020**, *250*, 112047.
43. Traganos, D.; Poursanidis, D.; Aggarwal, B.; Chrysoulakis, N.; Reinartz, P. Estimating satellite-derived bathymetry (SDB) with the google earth engine and sentinel-2. *Remote Sens.* **2018**, *10*, 859. [CrossRef]
44. Yu, D.; Hwang, C.; Andersen, O.B.; Chang, E.T.; Gaultier, L. Gravity recovery from SWOT altimetry using geoid height and geoid gradient. *Remote Sens. Environ.* **2021**, *265*, 112650. [CrossRef]
45. Sun, M.; Feng, W.; Yu, D.; Chen, X.; Liang, W.; Zhong, M. Analysing the impact of SWOT observation errors on marine gravity recovery. *Geophys. J. Int.* **2024**, *237*, 862–871. [CrossRef]

Disclaimer/Publisher's Note: The statements, opinions and data contained in all publications are solely those of the individual author(s) and contributor(s) and not of MDPI and/or the editor(s). MDPI and/or the editor(s) disclaim responsibility for any injury to people or property resulting from any ideas, methods, instructions or products referred to in the content.